Preprint

Design and In-Flight Analysis of an Electric Aircraft's Battery Thermal Management System

Citation

S. S. Shekar and M. A. Clarke, "Design and In-Flight Analysis of an Electric Aircraft's Battery Thermal Management System," 2024 IEEE Transportation Electrification Conference and Expo (ITEC), Chicago, IL, USA, 2024, pp. 1-8, doi: 10.1109/ITEC60657.2024.10598998.

1 Introduction

Aviation alone accounts for 2.5% of CO2 emissions and 1.9% of greenhouse gas emissions [1]. With 15% of all trips in the US being less than 200 miles, catering to 39 million travelers each year [2], radical changes are needed to achieve the goal of net zero carbon emissions by 2050 [3]. One such vision is to develop all-electric aircraft capable of decongesting our cities and having minimal environmental impact. Unlike conventional aircraft, where performance is influenced by the temperature of the working fluid, i.e., air, electric aircraft face unique challenges, requiring the expulsion of excess heat to prevent thermal runaway. Batteries remain the Achilles' heel of electrified aircraft propulsion despite remarkable advancements. Optimal thermal management of electrochemical and electromechanical systems is critical for achieving ideal performance and safe operation of all-electric vehicles (EVs), particularly for electric aircraft equipped with electro-propulsive architectures and power electronics. Throughout this article, we aim to answer two critical questions that have arisen in recent times within the relatively young electrochemical energy storage thermal management aerospace community:

1. At the conceptual level, what considerations and subsequent design methodologies should be employed when developing an electric aircraft's battery thermal management system?

2. How does the performance of an integrated battery thermal management system onboard an electric aircraft evolve during a full mission flight simulation?

To answer these research questions, Section 2 first outlines the system analyses conducted in this study. Section 3 then delves into the methodology of creating a thermal management system and Section 4 explores its performance during flight. In a recent article, Buticchi et al. [4] commented, "A paradigm shift, which consists of a holistic approach to system design, is necessary. Given the extremely close relationship between power electronics and thermal design, the manufacturing and integration aspects must be considered in the initial design stages." This philosophy aligns with implementing a detailed thermal management system design with RCAIDE, a next-generation, Python-based, open-source vehicle design environment for modeling, analyzing, and optimizing aerospace systems.

1.1 State of Aircraft Electrification

As observed from the failures of Airbus' E-Fan X [5] and NASA's X-57 tech demonstrators [6] to meet project milestones, insufficient attention to thermal management, fault detection, and aerodynamic performance penalties due to cooling can prove to be detrimental. To date, most research efforts exploring aviation electrification have been directed toward energy feasibility [7–10]. The current state of Battery Thermal Management System (BTMS) design is still in its infancy, with only a few studies that comprehensively account for how to design a thermal management system that regulates the battery temperature by either active cooling or heating [11, 12]. Previous works by Chapman et al. [13] and Clarke [14] discuss semi-empirical models for assessing eVTOL performance over operational lifetimes, focusing on cycle discharging, air cooling, and cell aging. Zhao et al. [15] performed extensive studies to understand the performance of a BTMS under

varying operating conditions. In the commercial realm, advances are being made in improving the performance of heat exchangers, with companies such as Honeywell developing a microchannel heat exchanger for a fuel-to-air application [16], and Boeing who is leveraging advances in manufacturing technologies to come up with advanced fin geometries that increase the thermal performance of a heat exchanger [17]. This article expands on previous work by outlining the process of sizing a BTMS from scratch, integrating elements such as a heat acquisition system (HAS) and a heat exchanger system (HEX) with the necessary auxiliary equipment needed to answer the research questions posed. It aims to provide an all-inclusive understanding of the challenges posed by different stages of the flight profile of aircraft proposed for regional and urban air mobility.

2 Aircraft Systems Modeling

2.1 Modeling Software

The Research Community Aerospace Interdisciplinary Design Environment (RCAIDE) is a computational research tool that aids in conceptualizing sustainable aerospace systems at a fraction of the cost of more memory-intensive, high-fidelity computer simulation tools. This tool is the successor to the SUAVE code [18], originally developed at Stanford University. Figure 1 describes a list of capabilities used to simulate electric aircraft. Collectively, these computational methods form the core of the mission solver, coupling flight physics with conservation equations to predict flight behavior at each Chebyshev collocation control point defining the flight segments of the mission. In this article, we will delve into the development of the thermal management subsystem and evaluate its performance across each collocation point in a given flight segment.

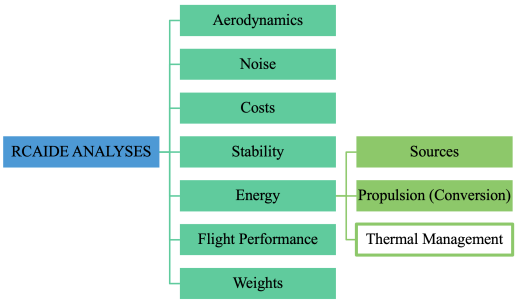

Figure 1: Analysis capabilities of RCAIDE.

2.2 Twin-Propeller Electric Commuter Aircraft

Shown in Fig. 2, the aircraft model used as the computational testbed for this study was inspired by the second modification variant of the NASA X-57 Maxwell, which itself was developed by retrofitting a Tecnam P2006T with an electric powertrain. This aircraft is powered by a lithium-ion NMC battery pack comprising 15 isolated modules, each with 8400 18650 Panasonic cells [19]. Each module is arranged in a 70-series, 120-parallel arrangement. The thermal characteristics of the battery cell are taken from correlations developed by Jeon et al. [20]. Additionally, each is assumed to be a thermal

lumped mass; the internal temperature gradient across the electrode-electrolyte-conductor layers within the jelly-rolled cells is neglected. The mission profile comprises 12 flight segments depicted in Fig. 3. The heat generated within the modules is based on the aircraft's power draw and external environmental factors.

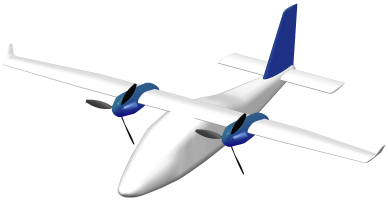

Figure 2: Twin-propeller electric commuter aircraft.

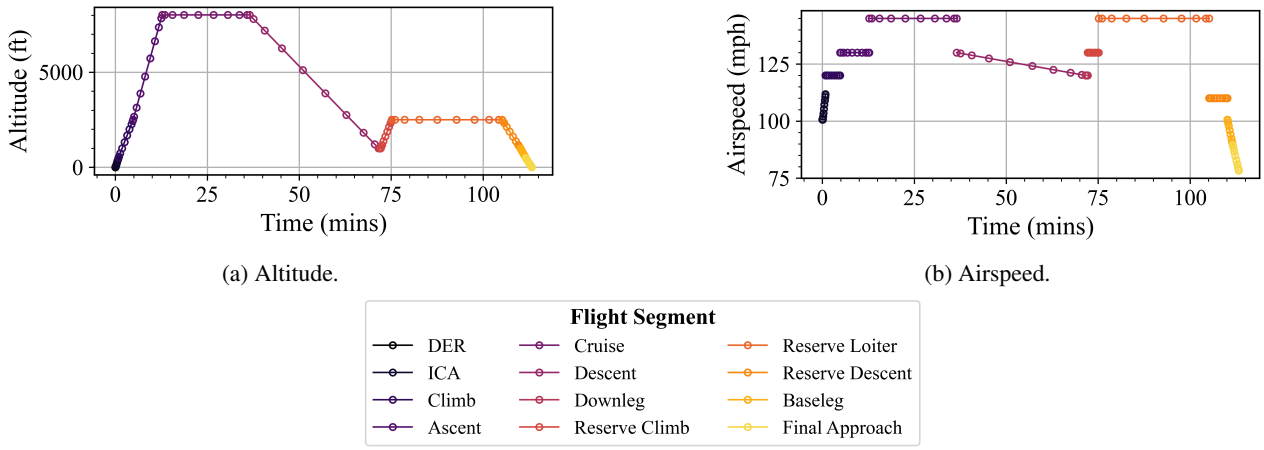

(a) Altitude.

(b) Airspeed.

Figure 3: Flight profile of the eCTOL as solved by RCAIDE

2.3 Battery Thermal Management System

A well-detailed thermal management system for an electric aircraft's battery pack would consist of the following components: 1) a heat acquisition system (HAS); 2) a heat exchanger system (HEX); 3) heating elements; 4) a reservoir tank that supplies coolant 5) pumps; 6) regulating values; 7) fans; and 8) lines for transporting the working fluid. These components were designed to collectively extract the maximum possible heat generated by the batteries, which, for this conventional takeoff and landing aircraft, is considered here to occur at the top of the climb. Despite being shown in Fig 4, the heating element is not used in this particular flight scenario under study since the aircraft does not reach altitudes that necessitate the need to warm up the batteries.

The HEX possesses two inlets, one for a fan and the other for a variable-area ram inlet. The former ensures that the HEX has sufficient air mass flow at low speeds, such as ground operation, while the ram inlet regulates airflow at high speeds during flight. The sizing of these systems is performed with the aid of RCAIDE's optimization framework, Nexus, which can handle single and nested optimization tasks and employ varying fidelities of different types of analyses, making it ideal for the conceptual design. During each function evaluation in the optimizer, there is a flow of information through

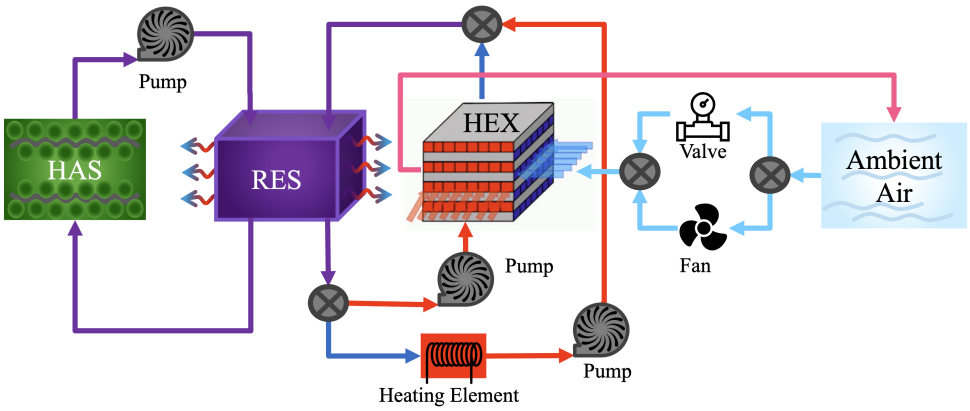

Figure 4: Battery thermal management system of an electric aircraft.

the Nexus framework. Once initialized, inputs from the optimizer are fed into RCAIDE, which functions as a "black box." Nexus then updates parameters and queries sensitivities to arrive at a solution. Objective function evaluations and, if applicable, constraint violations are then passed back as outputs to the optimizer via the Nexus.

3 BTMS Design Methodology

3.1 Heat Acquisition System Sizing

The HAS comprises wavy channels that pass through the rows of cells of each module. This cooling method is akin to the "Bandolero Roll" method [21], which is suggested to be one of the more efficient methods of heat extraction from batteries. The coolant flowing through is considered to be a 50-50 mixture of water and glycol. Outlined in (1), the HAS design procedure's objective is the minimization of HAS mass and the pump power required to generate the required pressure difference across the wavy channel that will ensure the extraction of sufficient heat (Q_{con}) generated by the battery (Q_{gen}). An additional objective during HAS sizing is the minimization of overall module dimensions. This is achieved by including the normal and parallel spacing between the cells, denoted x_n and x_p, respectively. The design variables of this optimization problem are the mass flow rate of the coolant ($\dot{m}_c$) and the geometric properties of the wavy channel, such as width (w), thickness (d) and the contact angle to the cells (θ) as shown in Fig. 5.

$$\begin{aligned} &\underset{M_{HAS}, P_{HAS}, x_n, x_p}{\text{minimize}} \quad f(\dot{m}_c, w, d, \theta) \\ &\text{s.t.} \quad Q_{gen} = Q_{con} \\ &\qquad\quad w - 2d > 0.01\text{m} \end{aligned} \tag{1}$$

For a given set of design parameters, the heat removed by the wavy channel can be determined via the equations below. The Reynolds Number is first calculated using (2). Then, the corresponding friction factor and Nusselt numbers are determined with the aid of (3) and (4) where γ is the aspect ratio of the channel [22]. Additionally, the length and area of the channel are computed based on the battery's geometric properties.

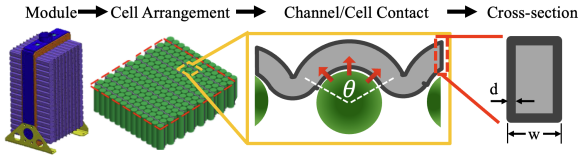

Figure 5: Wavy channel heat acquisition system.

$$Re = \frac{\rho d_h v}{\mu} \tag{2}$$

$$f = \begin{cases} \frac{24}{Re}(1 - (1.3553\gamma) + (1.9467(\gamma^2)) & \\ \quad -(1.7012(\gamma^3)) + (0.9564(\gamma^4)) & \\ \quad -(0.2537(\gamma^5))) & \text{if } Re < 2300 \\ 0.0791(Re^{-0.25})(1.8075 - 0.1125\gamma) & \text{if } Re \geq 2300 \end{cases} \tag{3}$$

$$Nu = \begin{cases} 8.235(1 - (2.0421\gamma) + (3.0853(\gamma^2)) & \\ \quad -(2.4765(\gamma^3)) + (1.0578(\gamma^4)) & \\ \quad -(0.1861(\gamma^5))) & \text{if } Re < 2300 \\ \frac{f}{2}(Re - 1000)\text{Pr} & \\ \left(1 + 12.7\left(\frac{f}{2}\right)^{0.5}(\text{Pr}^{\frac{2}{3}} - 1)\right) & \text{if } Re \geq 2300 \end{cases} \tag{4}$$

The corresponding heat transfer coefficient, h, is subsequently computed for the wavy channel (5), which is then used to calculate the number of Transfer Units (NTU) in (7). The outlet temperature of the coolant can then be computed as a function of NTU by (8). The heat removed is then computed by (10) after computing the logarithmic mean temperature in (9).

$$h = \frac{k \cdot Nu}{d_h} \tag{5}$$

$$U_{total} = \frac{1}{\left(\frac{1}{h}\right) + \left(\frac{d}{k_{chan}}\right)} \tag{6}$$

$$NTU = \frac{U_{total} \cdot A_{chan}}{\dot{m}_c \cdot c_p} \tag{7}$$

$$T_o = ((T_{\text{bat}} - T_i) \cdot (1 - \exp(-NTU))) + T_i \tag{8}$$

$$T_{\text{lm}} = \frac{(T_{\text{bat}} - T_i) - (T_{\text{bat}} - T_o)}{\ln\left(\frac{T_{\text{bat}} - T_i}{T_{\text{bat}} - T_o}\right)} \tag{9}$$

$$\dot{Q}_{con} = U_{\text{total}} \cdot A_{\text{chan}} \cdot T_{\text{lm}} \tag{10}$$

Finally, HAS mass and power can be computed by (11), where ρ_{line} is the density of the wavy channel, and dp is the pressure drop across the wavy channel obtained from (3). The normal and parallel spacing within each battery module is determined using (12) and (13) where d_{cell} is the diameter of the cell. These four quantities are combined to create a single objective via the weighted sum method.

$$M_{HAS} = \rho_{line} \cdot L_{chan} \quad \& \quad P_{HAS} = \frac{\dot{m}_c \cdot dp}{\eta_{tpump} \cdot \rho_c} \tag{11}$$

$$x_n = 2 \times (d_{\text{cell}} + w) \times \sin\left(\frac{\theta}{2}\right) \tag{12}$$

$$x_p = (d_{\text{cell}} + w) \times \cos\left(\frac{\theta}{2}\right) \tag{13}$$

3.2 Heat Exchanger System Sizing

For this study, a cross-flow gas-liquid HEX configuration was selected. Similar to the HAS, the HEX sizing methodology entails the minimization of mass and consumed power as a function of the mass flow rate of air and coolant $(\dot{m}_a, \dot{m}_c)$ and their respective inlet pressures (P_a, P_c), such that the length,(L), width,(W) and height,(H), of the HEX is limited to the aircraft's fuselage constraints as shown in (14). A specific surface designation for a flat plate cross-flow HEX is selected as a fundamental input, drawing upon relevant data such as finned area density and fin thickness [23].

$$\begin{aligned} &\underset{M_{HEX}, P_{HEX}}{\text{minimize}} \quad f(\dot{m}_c, \dot{m}_a, P_a, P_c) \\ &\text{s.t.} \quad L, W, H < 2.0\text{m} \end{aligned} \tag{14}$$

The determination of the dimensions of the HEX is in itself an iterative process. First, the coolant and air outlet temperatures are determined by (15) with an initial effectiveness(ε) of 0.85. The minimum $(C_{\min})$ and maximum $(C_{\max})$ heat capacities are subsequently determined to calculate the heat capacity ratio $(C_r = C_{\min}/C_{\max})$.

$$\begin{aligned} T_{o_c} &= T_{i_c} - \varepsilon(T_{i_c} - T_{i_a}) \quad \text{and} \\ T_{o_a} &= T_{i_a} + \left(\frac{\varepsilon \times \dot{m}_h}{\dot{m}_c}\right)(T_{i_h} - T_{i_c}) \end{aligned} \tag{15}$$

Using the effectiveness-NTU method, the number of transfer units can be evaluated from (16) [22] using SciPy's root

solver [24].

$$\varepsilon = 1 - \exp\left(\frac{\left(\text{NTU}^{0.22}\right)}{C_r} \cdot \left(\exp\left(-C_r \cdot \left(\text{NTU}^{0.78}\right)\right) - 1\right)\right) \tag{16}$$

To compute the initial core mass velocity using (17), the assumptions include $j_{f_{c,a}} = 0.25$, $ntu_c = 2NTU$, and $ntu_a = 2C_rNTU$. Additionally, the initial fin efficiencies are assumed to be 0.8, as indicated in the design methodology described by Shah et al. [25].

$$G_{c,a} = \sqrt{2\rho_{m_{c,a}} \frac{\delta_{p_{c,a}}}{(Pr_{c,a})^{2/3}} \frac{\eta_{o_{c,a}} j_{f_{c,a}}}{ntu_{c,a}}} \tag{17}$$

Based on the Reynolds Number derived from the core mass velocities computed in (17), the Colburn and Friction factors are updated on the basis of empirical relations (18) and (19) obtained from [23].

$$j_{a,c} = 0.0131(Re_{a,c}/1000)^{-0.415} \tag{18}$$

$$f_{a,c} = 0.0514(Re_{a,c}/1000)^{-0.471} \tag{19}$$

Furthermore, the fin efficiency is reevaluated in (23) for both the hot and cold sides of the HEX. This reassessment is based on the heat transfer coefficients derived in (20), providing a more accurate depiction of the fin efficiency under updated thermal conditions.

$$h_{c,a} = j_{c,a} G_{c,a} c_{p_{c,a}} (Pr_{c,a})^{2/3} \tag{20}$$

$$(m_f)_{c,a} = \sqrt{\frac{2h_{c,a}}{k_f \delta_{c,a}} \left(1 + \frac{\delta_{c,a}}{l_{s_{c,a}}}\right)} \tag{21}$$

$$(l_f)_{c,a} = \frac{b_{c,a}}{2} - \delta_{c,a} \tag{22}$$

$$(\eta_f)_{c,a} = \frac{\tanh((m_f)_{c,a}(l_f)_{c,a})}{(m_f)_{c,a}(l_f)_{c,a}} \tag{23}$$

Neglecting fouling effects for simplicity, the overall heat transfer coefficient can be evaluated by (24). The length along the coolant entrance and the air entrance are evaluated from (25) using the surface free flow area and the minimum free flow area. The height of the stack can also be computed from (26), where $A_{f_{c,h}}$ is the core frontal area.

$$U = \frac{1}{\frac{1}{\eta_{o_c} h_c} + \frac{\alpha_a/\alpha_c}{\eta_{o_a} h_a}} \tag{24}$$

$$L, W = \frac{d_{h_{c,a}} A_{c,a}}{4A_{o_{c,a}}} \tag{25}$$

$$H = \frac{A_{f_{c,h}}}{L, W} \tag{26}$$

The resulting pressure differences of the coolant and air sections are evaluated from (30), where $\sigma_{a,c}$ is the ratio of the minimum free-flow area to the frontal area. Note that the friction factor is corrected (29) to account for the effect of wall temperature (28). The entrance and exit coefficients are evaluated to be as follows: $K_{c_{c,a}} = 0..36$ & $K_{e_{c,a}} = 0.42$ [23]

$$R_{a,c} = \frac{1}{\eta_{o_{a,c}} h_{a,c} A_{a,c}} \tag{27}$$

$$T_w = \frac{T_{m_a} + \frac{R_a}{R_c} T_{m_c}}{1 + \frac{R_a}{R_c}} \tag{28}$$

$$f_{wall_{(a,c)}} = f_{a,c} \left(\frac{T_w}{T_{m_{a,c}}} \right)^{0.81} \tag{29}$$

$$\begin{aligned} \Delta P_{\text{new}_{(a,c)}} =& \frac{G_{a,c}^2}{2\rho_{a,c_i}} \left((1 - \sigma_{a,c}^2 + k_{a_{a,c}}) + 2 \left(\frac{\rho_{a,c_i}}{\rho_{a,c_o}} - 1 \right) \right) \\ &+ f_{a,c\_wall} \cdot 4 \frac{L_{a,c}}{d_{c,a}} \frac{\rho_{a,c_i}}{\rho_{a,c_m}} \\ &- (1 - \sigma_{a,c}^2 - k_{e_{a,c}}) \frac{\rho_{a,c_i}}{\rho_{a,c_o}} \end{aligned} \tag{30}$$

The pressure difference obtained is compared to the limiting pressure ratio, typically given by the pump manufacturer. This sizing process is repeated by calculating core mass velocities using (17) with the new pressure differential until the pressure differential between two successive iterations falls under 0.01Pa. Once convergence is achieved, the dimensions obtained are cross-referenced to the constraints defined. The mass and power consumed by the HEX can finally be determined using (31) and (32), respectively.

$$M_{HEX} = \rho_{HEX} \cdot V_{HEX} \cdot (1 - \sigma_a - \sigma_c) \tag{31}$$

$$P_{HEX} = \frac{\dot{m}_c \Delta P_c}{\eta_{pump} \rho_{c_m}} + \frac{\dot{m}_h \Delta P_a}{\rho_{a_m}} \tag{32}$$

3.3 Reservoir

A central reservoir made of polyetherimide is modeled to simulate the supply of water-glycol coolant to the HAS and HEX. Assuming it is in the unpressurized, uninsulated portion of the cabin, it is exposed to ambient temperatures, and consequently, heat transfer through conduction, natural convection, and radiation must be considered as seen in (33), with a heat transfer coefficient of $10 W/m^2 K$ This consideration is crucial for accurately capturing temperature changes with increasing altitude, as defined by the International Standard Atmosphere model [26].

$$\frac{dQ}{dt}_{\text{cond}} = \frac{KA\Delta T}{d}, \quad \frac{dQ}{dt}_{\text{conv}} = hA\Delta T \quad \& \quad \frac{dQ}{dt}_{\text{rad}} = \sigma A(\varepsilon_{\text{res}} T_{\text{res}}^4 - \varepsilon_{\text{air}} T_{\text{air}}^4) \tag{33}$$

4 BTMS Performance

Equipped with a fully designed BTMS for the commuter aircraft, we now focus on simulating a complete flight profile. Since the BTMS was sized to extract heat at the point of maximum power draw, unregulated operation during less power-intensive flight segments would overcool the battery cells and place them outside their optimal thermal range. If the temperature falls below the lower threshold, the electrochemical reaction rate that generates the potential difference with the cell decreases, impacting its electrical circuit properties. Additionally, continuously running the BTMS at the design conditions will drain the battery pack prematurely. Therefore, to avoid such circumstances without implementing a complicated control algorithm, the BTMS is operated at prescribed percentages of its design condition during flight. These are provided in Fig. 6. As shown in Fig. 4, the HEX possesses a dual inlet configuration. This allows us to control the quantity of air entering the system. At high speeds, the ram inlet is adjusted from fully open (100%) to closed (0%) to regulate the mass flow of the air into the HEX. During segments where the aircraft's velocity is low, the fan is turned on to pull air into the HEX. This fan is also operated in anticipation of an emergency or during the end of the flight to ensure that the batteries are within their operating window for subsequent flights. It is assumed during these periods that the ram inlet remains closed, resulting in no cooling drag.

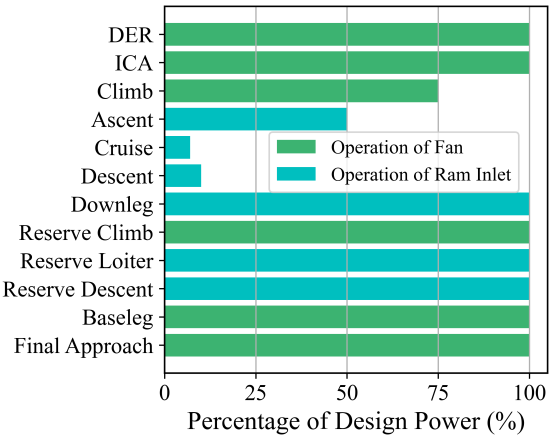

Figure 6: Operational conditions the fan and ram inlet.

4.1 Reservoir

At each time step, the reservoir temperature is updated, taking into consideration the heat loss to the environment and the resulting temperature with the coolant flowing into the reservoir from the HAS and HEX computed at each time step from (34) as listed in [22]. Exposure to the environment at high altitudes makes the drop in the reservoir coolant temperature significant. This aids in cooling the battery pack without requiring much power from the HEX and the HAS. Hence, the

BTMS in the cruise and descent segments can operate at less than 10% of its rated power.

$$T_{final} = \frac{[(\dot{m}_c dt)c_p T]_{HAS} + [(\dot{m}_c dt)c_p T]_{HEX}}{m_c c_p} + \frac{[(m_{res} dt)c_p T]_{RES}}{m_c c_p} \tag{34}$$

To convey the impact of adding a reservoir that is exposed to environmental factors, Fig. 7 presents a hypothetical scenario in which an aircraft is simulated with ($w/Res.$) and without ($w/oRes.$) a reservoir integrated into the BTMS network. Note that in both cases, the reservoir is onboard the aircraft. The HAS can leverage the sizeable temperature difference between the battery cells within the module and coolant within an isolated reservoir, i.e., the $w/oRes.$ case. The result of such coupling is the $w/Res.$ case, as shown in the figure.

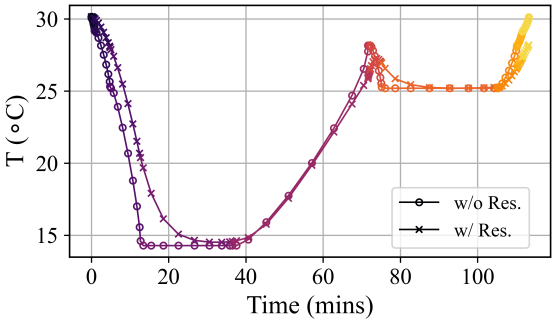

Figure 7: Reservoir coolant temperature.

4.2 Heat Acquisition System

Based on the mass flow rate of the coolant at each time step, the power consumed during flight is determined using (11). The net heat removal is determined by (35), from which the temperature gradient is derived using (36), incorporating the physical properties of the battery pack. Given in (37), the future cell temperature (T_{i+1}) is obtained based on its current state (T_i). This updated battery temperature is then utilized in the mission solver at each time step to evaluate the electrochemical discharge properties of the cells within the battery pack. The changes in power consumption by the HAS as a function of the input mass flow rate are depicted in Fig. 8.

$$\dot{Q}_{net} = \dot{Q}_{gen} - \dot{Q}_{con} \tag{35}$$

$$\frac{dT}{dt} = \frac{\dot{Q}_{net}}{N_{cell} C_{p_{cell}} m_{cell}} \tag{36}$$

$$T_{i+1} = \frac{dT}{dt} + T_i \tag{37}$$

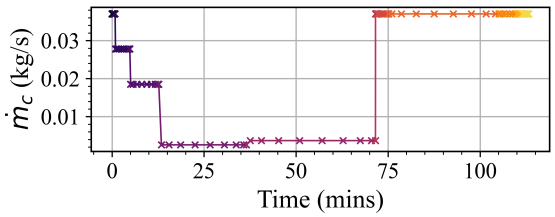

(a) Coolant mass flow rate in wavy-channel HAS.

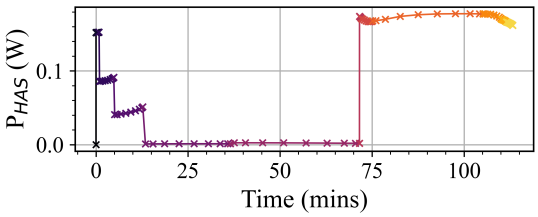

(b) Heat acquisition system power consumption.

Figure 8: HAS operating conditions.

4.3 Heat Exchanger System

Mirroring the HAS process, the HEX operating conditions are computed at each time step. Its power consumption is calculated using (32), derived from the operating pressure differentials elucidated in (30). Figure 9 shows the coolant and air mass flow rates. An expected spike in power consumption is observed when the fan is engaged.

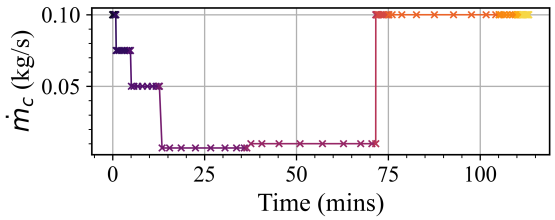

(a) Coolant mass flow rate within HEX.

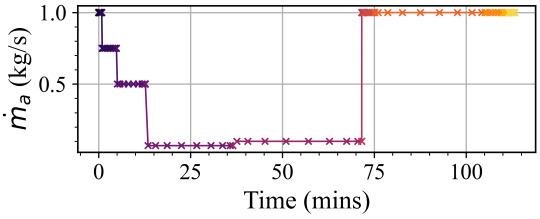

(b) Air mass flow rate within HEX.

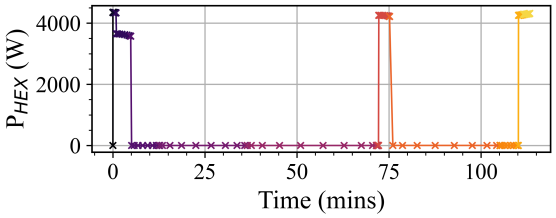

(c) HEX power consumption.

Figure 9: Heat exchanger operating conditions.

When the ram-inlet is used, its contribution to the total drag shown in Fig. 10 can be computed using (38) as described by Brelje et al. [27]. Here we see that adding the BTMS necessitates additional power from the battery to achieve the specified flight kinematics shown in Fig. 3.

$$F_{cooling} = \dot{m}(U_e C_{fg} - U_\infty) + A_e C_{fg}(p_e - p_\infty)) \tag{38}$$

4.4 Aircraft Flight Performance

This additional power from the HEX and HAS draw leads to further heat generation in the battery pack and changes operating conditions. Comparing the battery conditions with and without a BTMS reveals key insights. Without the BTMS, the end-of-flight state of charge of the battery is 0.14, whereas with the BTMS, it is 0.10. Moreover, without a BTMS, there is an 11°C increase in temperature, whereas, with a BTMS, the battery pack is maintained within a 5°C

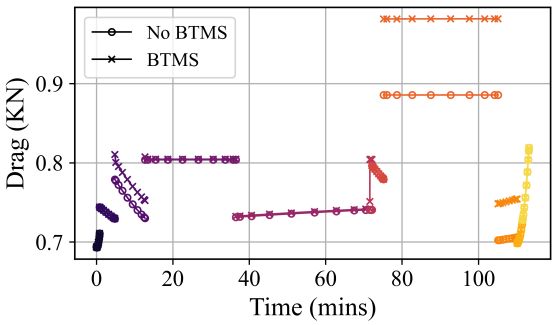

Figure 10: Aircraft total drag.

window, considered an ideal operating condition for the employed battery pack [28]. These findings help to shed light on what would be required to size battery packs for electric aircraft more accurately. Given a desired range, the aircraft designer must account for the power draw to cooling and its associated aerodynamic penalty.

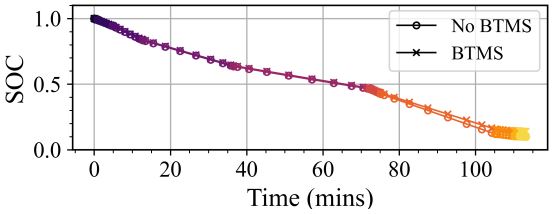

(a) State of charge.

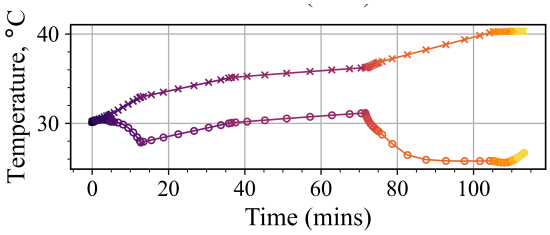

(b) Battery cell temperature.

Figure 11: Battery temperature and state of charge.

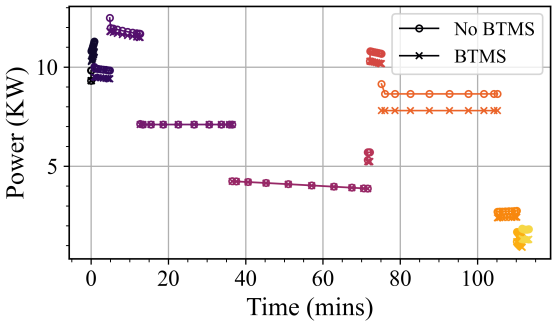

Figure 12: Power consumed by the battery pack.

5 Conclusion

This article presents a detailed design methodology for the conceptual design of a BTMS. The designed BTMS was integrated into an electric aircraft to study its behavior under realistic flight conditions. The results are structured to answer the initial research questions:

1. At the conceptual level, what considerations and subsequent design methodologies should be employed when developing an electric aircraft's battery thermal management system?

2. How does the performance of an integrated battery thermal management system onboard an electric aircraft evolve during a full mission flight simulation?

The designed BTMS successfully maintains the battery pack's temperature within a 5° C window, ensuring efficient battery operation. A decrease in reservoir coolant temperature at high altitudes effectively cools the battery pack, reducing the reliance on the HEX. As a result, during the cruise and descent segments, the BTMS can operate efficiently using less than 10% of its total power capacity. Furthermore, the study highlights the importance of considering thermal management early in the design process of electric aircraft, emphasizing the need for a holistic approach to system design that encompasses thermal considerations alongside other performance metrics. In conclusion, the developed BTMS not only meets the performance criteria but lays the groundwork for studying trends in electric aircraft design, paving the way for more sustainable and efficient aviation solutions.

6 Future Perspective

The design procedure for battery temperature control is crucial for advancing electric aircraft technology. With the increasing emphasis on electric aircraft, there's a demand to integrate thermal management for all components into a comprehensive mission solver. This involves analyzing diverse conditions like cold starts and thermal failure modes to create an efficient thermal management system. Looking ahead, more complex thermal management architectures than those described in this article need to be conceptualized and tested against the load profiles of electric aircraft. Additionally, advancements in thermal management technologies, such as phase change materials and active cooling systems, should be explored for their applicability in enhancing the thermal performance of electric aircraft systems. This holistic approach to thermal management will play a crucial role in the continued development and adoption of electric aircraft for sustainable aviation.

References

[1] H. Ritchie, "Climate change and flying: what share of global co2 emissions come from aviation?" *Our World in Data*, 2020, https://ourworldindata.org/co2-emissions-from-aviation.

[2] Bureau of Transportation Statistics (BTS), "Bureau of Transportation Statistics (BTS) - Download Data," https://www.transtats.bts.gov/DL_SelectFields.aspx?gnoyr_VQ=GED&QO_fu146_anzr=Nv4%20Pn44vr45, 2023, [Online].

[3] I. A. T. A. (IATA), "IATA FlyNeutral Initiative," https://www.iata.org/en/programs/environment/flynetzero/, 2023, [Online].

[4] G. Buticchi, P. Wheeler, and D. Boroyevich, "The more-electric aircraft and beyond," *Proceedings of the IEEE*, vol. 111, no. 4, pp. 356–370, 2023.

[5] J. Excell, "Rolls-royce and airbus cancel e-fan x project," Apr 2022. [Online]. Available: https://www.theengineer.co.uk/content/news/rolls-royce-and-airbus-cancel-e-fan-x-project/

[6] P. Brinkmann, "X-57 team probes safety question that ended development without a flight," Jul 2023. [Online]. Available: https://aerospaceamerica.aiaa.org/x-57-team-probes-safety-question-that-led-nasa-to-end-development-of-the-electric-aircraft-without-ever-flying-it/

[7] W. Liu, Z. Deng, J. Li, and X. Hu, "Investigating the electrothermal behavior of evtol batteries in urban air mobility applications," in *2022 IEEE 25th International Conference on Intelligent Transportation Systems (ITSC)*, 2022, pp. 40–45.

[8] X.-G. Yang, T. Liu, S. Ge, E. Rountree, and C.-Y. Wang, "Challenges and key requirements of batteries for electric vertical takeoff and landing aircraft," *Joule*, vol. 5, no. 7, pp. 1644–1659, 2021.

[9] M. Warren, A. Garbo, M. T. Kotwicz Herniczek, T. Hamilton, and B. German, "Effects of range requirements and battery technology on electric vtol sizing and operational performance," in *AIAA SciTech 2019 forum*, 2019, p. 0527.

[10] M. A. Clarke and J. Alonso, "Evaluating the performance and acoustic footprint of aircraft for regional and urban air mobility," in *AIAA Aviation 2021 Forum*, 2021, p. 3205.

[11] J. Harrison, D. Charles, J. Zenker, and E. Frank, "Using multi-physics system simulation to predict battery pack thermal performance and risk of thermal runaway during evtol aircraft operations," in *2019 AIAA/IEEE Electric Aircraft Technologies Symposium (EATS)*, 2019, pp. 1–13.

[12] C. Zhao, M. Clarke, H. Kellermann, and D. Verstraete, "Liquid cooling systems for batteries of electric vertical takeoff and landing aircraft," *Journal of Aircraft*, vol. 0, no. 0, pp. 1–17, 0. [Online]. Available: https://doi.org/10.2514/1.C037404

[13] J. W. Chapman, S. L. Schnulo, and M. P. Nitzsche, "Development of a thermal management system for electrified aircraft," *AIAA Scitech 2020 Forum*, 1 2020.

[14] M. A. Clarke and J. J. Alonso, "Forecasting the operational lifetime of battery-powered electric aircraft," *Journal of Aircraft*, vol. 60, no. 1, pp. 47–55, 2023.

[15] C. Zhao, M. Clarke, H. Kellermann, and D. Verstraete, "Liquid cooling systems for batteries of electric vertical takeoff and landing aircraft," *Journal of Aircraft*, vol. 0, no. 0, pp. 1–17, 0. [Online]. Available: https://doi.org/10.2514/1.C03740

[16] M. Williams, A. Muley, J. Bolla, and H. Strumpf, "Advanced heat exchanger technology for aerospace applications," in *Power Systems Conference*. SAE International, nov 2008. [Online]. Available: https://doi.org/10.4271/2008-01-2903

[17] *Advanced Heat Transfer Devices for Aerospace Applications*, ser. ASME International Mechanical Engineering Congress and Exposition, vol. Volume 8: Heat Transfer and Thermal Engineering, 11 2017. [Online]. Available: https://doi.org/10.1115/IMECE2017-72382

[18] T. W. Lukaczyk, A. D. Wendorff, M. Colonno, T. D. Economon, J. J. Alonso, T. H. Orra, and C. Ilario, "Suave: an open-source environment for multi-fidelity conceptual vehicle design," in *16th AIAA/ISSMO Multidisciplinary Analysis and Optimization Conference*, 2015, p. 3087.

[19] Portable Rechargeable Battery Business Division, "Technical Information of NCR18650G," https://www.imrbatteries.com/content/panasonic_ncr18650g.pdf, SANYO Electric Co., Ltd, Tech. Rep. 13H06BZGMIT, ., [retrieved 30 Jan. 2020].

[20] D. H. Jeon and S. M. Baek, "Thermal modeling of cylindrical lithium ion battery during discharge cycle," *Energy Conversion and Management*, vol. 52, no. 8, pp. 2973–2981, 2011. [Online]. Available: https://www.sciencedirect.com/science/article/pii/S0196890411001439

[21] J. Harrison, D. Charles, J. Zenker, and E. Frank, "Using multi-physics system simulation to predict battery pack thermal performance and risk of thermal runaway during evtol aircraft operations," in *AIAA Propulsion and Energy 2019 Forum*. American Institute of Aeronautics and Astronautics, Aug. 2019. [Online]. Available: http://dx.doi.org/10.2514/6.2019-4406

[22] F. P. Incropera, *Fundamentals of heat mass transfer 4e wse + & interactive heat transfer V1.5 3e to accompany fundamentals of heat & mass stransfer 4e set*. Nashville, TN: John Wiley & Sons, Feb. 1998.

[23] W. Kays and A. London, *Compact heat exchangers*. Krieger Pub. Co., 1984. [Online]. Available: http://books.google.de/books?id=A08qAQAAMAAJ

[24] P. Virtanen, R. Gommers, T. E. Oliphant, M. Haberland, T. Reddy, D. Cournapeau, E. Burovski, P. Peterson, W. Weckesser, J. Bright, S. J. van der Walt, M. Brett, J. Wilson, K. J. Millman, N. Mayorov, A. R. J. Nelson, E. Jones, R. Kern, E. Larson, C. J. Carey, İ. Polat, Y. Feng, E. W. Moore, J. VanderPlas, D. Laxalde, J. Perktold, R. Cimrman, I. Henriksen, E. A. Quintero, C. R. Harris, A. M. Archibald, A. H. Ribeiro, F. Pedregosa, P. van Mulbregt, and SciPy 1.0 Contributors, "SciPy 1.0: Fundamental Algorithms for Scientific Computing in Python," *Nature Methods*, vol. 17, pp. 261–272, 2020.

[25] R. K. Shah and D. P. Sekulić, *Fundamentals of Heat Exchanger Design*. Wiley, Jul. 2003. [Online]. Available: http://dx.doi.org/10.1002/9780470172605

[26] U. S. N. Oceanic, A. Administration, and U. S. C. on Extension to the Standard Atmosphere, *U.S. Standard Atmosphere, 1976*, ser. NOAA - SIT 76-1562. National Oceanic and Amospheric [sic] Administration, 1976. [Online]. Available: https://books.google.com/books?id=x488AAAAIAAJ

[27] B. J. Brelje, J. P. Jasa, J. R. R. A. Martins, and J. S. Gray, "Development of a conceptual-level thermal management system design capability in OpenConcept," in *NATO Research Symposium on Hybrid/Electric Aero-Propulsion Systems for Military Applications (AVT-RSY-323)*, Trondheim, NO, Oct. 2019.

[28] X. Han, L. Lu, Y. Zheng, X. Feng, Z. Li, J. Li, and M. Ouyang, "A review on the key issues of the lithium ion battery degradation among the whole life cycle," *ETransportation*, vol. 1, p. 100005, 2019.